npj | climate and atmospheric science

Article

Published in partnership with CECCR at King Abdulaziz University

https://doi.org/10.1038/s41612-025-01076-y

Linking the subseasonal variability of the East Asia winter monsoon and the Madden-Julian Oscillation through wave disturbances along the subtropical jet

Junyi Xiu[1,2,3], Xianan Jiang[3] ✉ & Renhe Zhang[2] ✉

Despite an urgent demand for reliable subseasonal-to-seasonal (S2S) predictions to guide disaster preparedness, our current climate models show limited S2S prediction skill, particularly for precipitation, due to an inadequate understanding of the key processes that drive regional S2S variability. Here we demonstrate that the leading subseasonal variability mode of precipitation over the East Asian Winter Monsoon (EAWM) region is not only closely tied to the activity of the Madden-Julian Oscillation (MJO), but also linked to precipitation and temperature extremes worldwide, influenced by a circumglobal Rossby wave-train along the subtropical westerly jet. Despite a close phase-lock relationship between the MJO and subseasonal EAWM precipitation, our findings indicate that the MJO itself may only play a minor role in the subseasonal EAWM variability. Given its significant impact on the S2S variability of global weather extremes, we call for coordinated community efforts to enhance the understanding and prediction of the circumglobal Rossby wave-train.

Weather and climate extremes, such as heavy precipitation, severe droughts, heat waves, and cold spells, have tremendous environmental and socio-economic impacts. There is growing evidence that the occurrence patterns of these extreme events, including their frequency, intensity, location, and timing, have changed due to human-induced climate change[1]. As a result, accurate predictions of these extreme events with a lead time of 2 weeks to one season, known as subseasonal-to-seasonal (S2S) predictions, have become an active area of research, and an urgent need for disaster preparedness, risk management, and informing policy-making for climate mitigation[2–4].

In general, the strongest S2S variability in precipitation occurs in the tropics, often associated with the Madden-Julian Oscillation (MJO)[5,6]. Most recently, there has been an increasing community effort to explore the predictability of precipitation on S2S timescales in densely populated regions over the extratropics, such as East Asia, the west coast of North America, and the Mediterranean Sea Region[7–16]. For East Asia, while the strongest precipitation usually occurs during the summer monsoon season, extreme precipitation during winter, characterized as an active period of the East Asian Winter Monsoon (EAWM), can also result in severe meteorological hazards, including prolonged cold spells, freezing rain, and snowstorms.

The S2S variability in winter precipitation over East Asia is generally linked to the southward migration of circulation patterns over the mid-to-high latitudes of the Eurasian Continent[17–20], often accompanied by cold-air outbreaks, and/or influenced by the tropical MJO[19,21–26]. While the essential role of the MJO for the S2S variability of precipitation over East Asia has been recently questioned[17], a critical question remains unaddressed regarding the observed phase-lock relationship between subseasonal EAWM precipitation and MJO convection as previously reported[17,21,23,25,26]. Specifically, peak subseasonal EAWM precipitation is typically observed when enhanced MJO convection occurs over the Eastern Indian Ocean.

In this study, we illustrate that the fluctuations in EAWM precipitation and the activity of the MJO over the equatorial Indian Ocean tend to synchronize due to eastward-migrating Rossby wave disturbances along the subtropical jet stream, leading to a close phase-lock relationship between these two phenomena. The MJO itself, however, may only play a relatively minor role in driving the subseasonal variability of EAWM precipitation. This same Rossby wave-train pattern along the subtropical jet, which extends from the west coast of Europe to North America, links the subseasonal variability of EAWM to other densely populated extratropical regions, such as the west coast of North America and the Mediterranean Sea

[1]CMA Earth System Modeling and Prediction Center, China Meteorological Administration, Beijing, China. [2]Department of Atmospheric and Oceanic Sciences/Institute of Atmospheric Sciences, Fudan University, Shanghai, China. [3]Joint Institute for Regional Earth System Science and Engineering, University of California Los Angeles, Los Angeles, CA, USA. ✉e-mail: xianan@ucla.edu; rhzhang@fudan.edu.cn

Region. These findings have significant implications for improving S2S prediction of winter extreme events worldwide, for example, over the west coast of North America, where a breakthrough in S2S prediction of winter precipitation is urgently needed to guide local water managers coping with recent prolonged droughts[9,12].

Results

The leading subseasonal variability mode of precipitation associated with the EAWM

To identify the leading subseasonal variability mode of precipitation associated with the EAWM, we conducted an extended empirical orthogonal function (EEOF) analysis on the 10–90-day filtered anomalous precipitation from the Tropical Rainfall Measuring Mission (TRMM)[27] for the period from 1998 to 2016. This analysis focuses on the extended boreal winter (November-April) over the East Asia region (18°–37°N, 90°–140°E; red box at day 0 in Fig. 1a), where strong local S2S variability in precipitation has been previously reported[17,19,23]. The leading mode of subseasonal precipitation variability, with a prevailing period of about 25 days, is represented by the first pair of EEOF modes that are 90° out of phase (see "Methods" for details, also Supporting Figs. S1 and S2). Its evolution pattern can thus be illustrated using lag-regression patterns of the 10–90-day-filtered rainfall anomalies in relation to the time series of the principal component associated with the first leading EEOF mode (EPC_1).

The leading subseasonal mode of precipitation over East Asia is characterized by a north-south dipole pattern of anomalous rain belts that extend from Southeastern China to Japan/Korea, with a gradual southeastward propagation over time (Fig. 1a). The peak positive precipitation anomalies in this region occur on day 0, accompanied by southwesterly

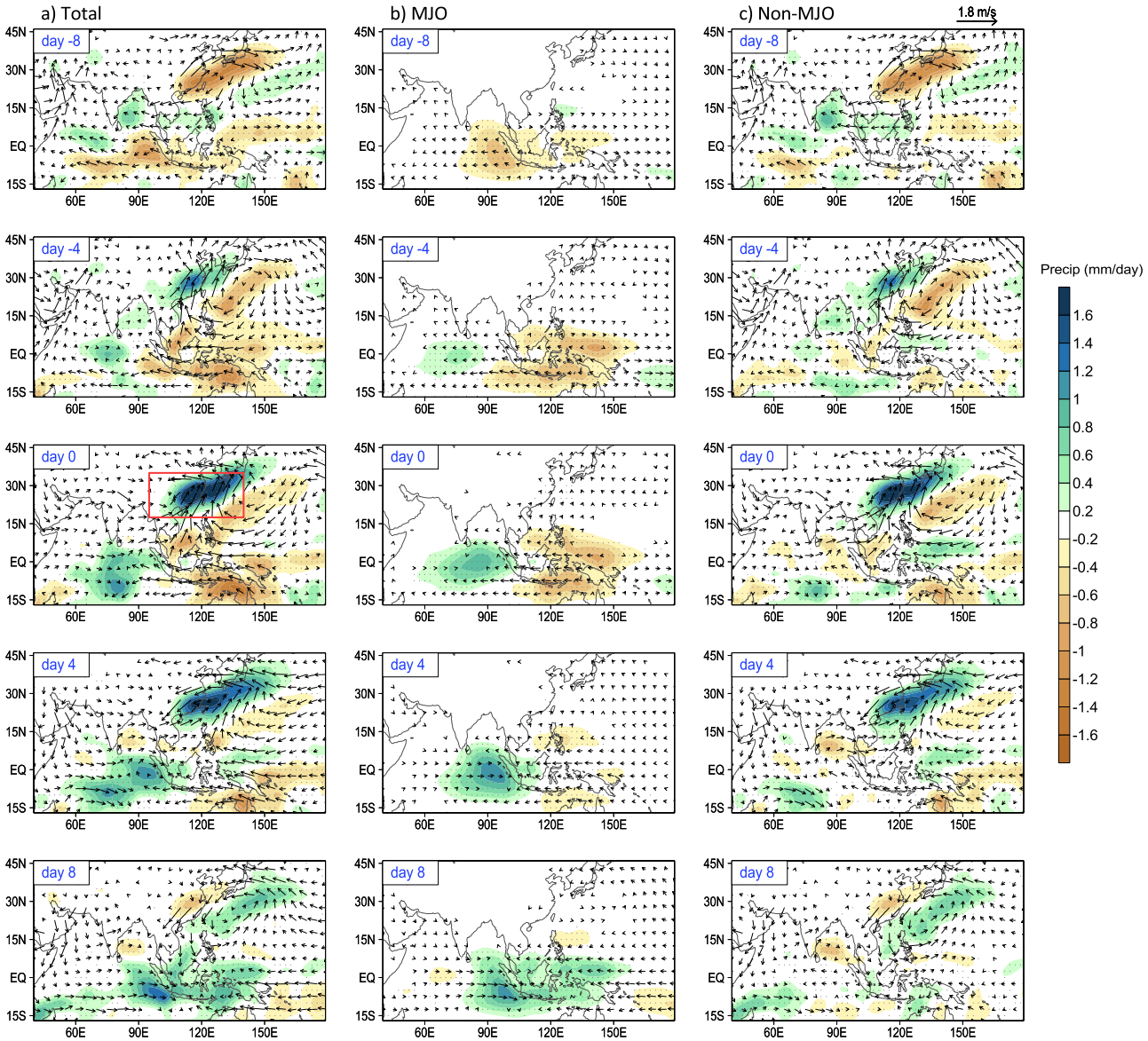

Fig. 1 | Evolution of anomalous precipitation and winds associated with subseasonal EAWM precipitation variability. Anomalous precipitation (shaded with the color bar on the right; units: mm day^{-1}; based on TRMM) and 850 hPa winds (vectors with the scale on the upper-right; speed less than 0.05 m s^{-1} are omitted) associated with the leading subseasonal precipitation variability mode over East Asia during boreal winter (left column, **a**). These evolution patterns are derived by lead-lag regressions of 10–90-day filtered precipitation and wind anomalies against the EPC_1 corresponding to the $EEOF_1$ mode of 10–90-day filtered winter precipitation over East Asia (the red box at day 0). The total anomalies on the left column are separated into MJO-related anomalies (middle column, **b**) and non-MJO anomalies (right column, **c**). Areas with dark gray dots indicate precipitation anomalies surpassing the 95% statistical significance level based on their corresponding correlation coefficients using the Student's *t*-test. See Methods for details on identifying the leading subseasonal EAWM precipitation mode and the separation of the MJO-related and non-MJO components.

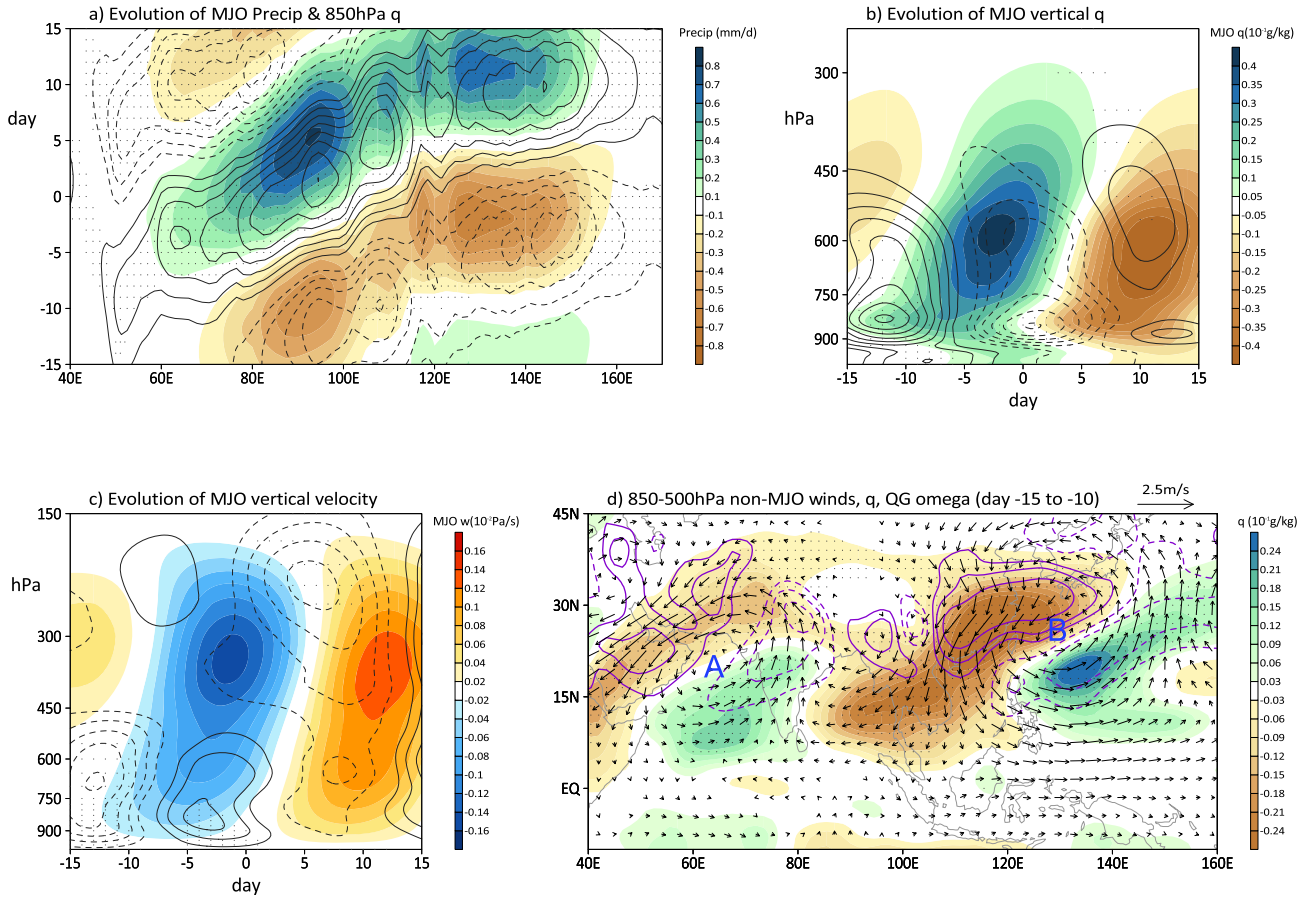

Fig. 2 | Initiation of the MJO over the western equatorial Indian Ocean associated with the EAWM precipitation variability. a Longitude–time evolution of MJO-related precipitation anomalies (shaded; units: mm day^{-1}; based on TRMM) and 850 hPa MJO-related specific humidity anomalies (q; contours with intervals of 0.1×10^{-1} g kg^{-1}, dashed if negative with zero contours omitted). Both variables are averaged over 15°S–15°N; (**b**) Pressure–time cross-sections of MJO-related (shaded with units of 10^{-1} g kg^{-1}) and non-MJO (contours with intervals of 0.2×10^{-1} g kg^{-1}, dashed if negative with zero contours omitted) specific humidity anomalies over the western equatorial Indian Ocean (55–65°E; 15°S–15°N); (**c**) similar to (**b**) but for MJO-related (shaded with units of 10^{-2} Pa s^{-1}) and non-MJO (contours with intervals of 0.03×10^{-2} Pa s^{-1}) vertical velocity anomalies; (**d**) 850–500 hPa vertically averaged non-MJO components of anomalous specific humidity (shaded; unit: 10^{-1} g kg^{-1}), winds (vectors; see the scale on the upper-right of the panel; vectors with wind speed less than 0.05 ms^{-1} omitted), and vertical p-velocity derived based on the quasi-geostrophic omega-equation (contours with intervals of 0.3×10^{-2} Pa s^{-1}, dashed if negative with zero contours omitted). The labels "A" and "B" denote centers of the two cyclones over the Arabian Sea and East Asia, respectively, along the circumglobal Rossby wave pattern. Areas with dark gray dots indicate anomalies surpassing the 95% statistical significance level for MJO q in (**a**), non-MJO q in (**b**, **d**), and non-MJO vertical velocity in (**c**), respectively.

anomalous low-level winds that converge onto the area of convection, with an anticyclone to the east and a cyclone to the west of the enhanced precipitation center (Fig. 1a). The southwesterly low-level winds, on one hand, transport abundant moisture from southern China and the western Pacific to support vigorous convection; on the other hand, the upward motion induced by the quasi-geostrophic circulation also plays a critical role in promoting enhanced convection over East Asia (to be discussed in Fig. 2). Notably, the anomalous precipitation and circulation patterns observed on day -8 largely mirror those on day 4, but with opposite signs, consistent with a period of ~25 days for the leading subseasonal mode of EAWM precipitation (Supporting Fig. S2).

Associated with the evolution of EAWM precipitation, the development of enhanced convection is observed over the western equatorial Indian Ocean near 60°E on day 8; it then gradually intensifies and propagates eastward along the equator towards the Maritime Continent after day 4 (Fig. 1a), exhibiting typical characteristics of the MJO. Between day 0 and day 4, strong precipitation occurs over East Asia as the enhanced MJO convection reaches the eastern equatorial Indian Ocean, corresponding to MJO Phase 3 according to the Wheeler-Hendon MJO index[28]. These results are largely in alignment with many previous studies that highlight the MJO's significant role in driving the subseasonal variability of EAWM precipitation[19,21–26].

Role of the tropical MJO for the subseasonal variability of EAWM precipitation

To quantify the contribution of the MJO to the leading mode of subseasonal variability in EAWM precipitation, we employed a regression-based approach to derive daily precipitation and circulation anomalies associated with the MJO (see "Methods"). By performing lag-regressions against the EPC_1 time series, we can obtain the evolution patterns of MJO-related precipitation and circulation anomalies linked to the leading subseasonal variability mode of EAWM precipitation (Fig. 1b).

The typical evolution of the MJO linked to the subseasonal variations in EAWM precipitation is clearly evident in Fig. 1b. It shows the onset of enhanced MJO convection over the western equatorial Indian Ocean before day -4, followed by its intensification and gradual eastward movement along the equator after day -4, and finally crossing the Maritime Continent after day 4. However, the precipitation and circulation anomalies related to the MJO are largely confined to the tropics and show rather weak signals over the EAWM region. This suggests that the MJO may not significantly contribute to the subseasonal variability of EAWM precipitation. Figure 1c further illustrates the evolution of the residual precipitation and circulation anomalies after removing the MJO signals from the total, highlighting the non-MJO signals linked to subseasonal precipitation variability over East Asia. The similarity in the evolution features of precipitation and circulation

anomalies over East Asia between Fig. 1a, c further confirms a relatively minor role of the MJO in driving the subseasonal variability of EAWM precipitation. Precipitation anomalies associated with the MJO explain about 10–15% of total 10–90-day precipitation variances over the EAWM region (Supporting Fig. S5). Further analysis indicates that the MJO's contribution to subseasonal variability of EAWM precipitation varies slightly throughout the winter months, ranging from a maximum contribution of ~18% in December to a minimum contribution of around 8% in March (figure not shown).

While this result largely aligns with the findings of Yao et al., which indicate that the MJO accounts for about 10% of subseasonal precipitation variability in East Asia, it contradicts many previous studies that highlight the critical role of the MJO in subseasonal variability of precipitation over the EAWM region. Differences are also noted between this study and Yao et al.: While Yao et al. (ref. 17; their Fig. 1a) found that enhanced subseasonal precipitation over Southern China is largely collocated with low-level cyclonic circulation, our analysis indicates that the anomalous positive precipitation center is typically located between an anticyclonic circulation to the east and a cyclonic circulation to the west (Fig. 1, day 0). Furthermore, the circumglobal Rossby-wave pattern related to subseasonal variability of EAWM precipitation, which will be further described below, was not evident in Yao et al., possibly due to an earlier generation of reanalysis dataset used in their study[17].

Triggering of the MJO by circulation patterns associated with EAWM precipitation

The strong link between increased subseasonal precipitation in East Asia with active MJO convection over the Indian Ocean, but the relatively minor role of the MJO in driving the subseasonal variability of EAWM precipitation, suggests that either the onset of tropical MJO convection is triggered by subseasonal EAWM variability, or that both the MJO and the subseasonal fluctuations in EAWM precipitation are influenced by shared large-scale factors. Previous research has suggested that subseasonal variability of the EAWM, such as the southward propagation of cold surges, can initiate tropical convection and the MJO, particularly over the western Pacific and Maritime Continent regions[17,29–31]. In contrast, the initiation of MJO convection, as illustrated in Fig. 1b, occurs over the western equatorial Indian Ocean before day -4. In this section, we will closely investigate the detailed processes that lead to MJO initiation over the western equatorial Indian Ocean in relation to the evolution of subseasonal variability of EAWM precipitation.

Figure 2a illustrates the time-longitude evolution of MJO-related precipitation anomalies along the equator, based on the lag-regression patterns shown in Fig. 1b (shaded). The eastward propagation of the MJO associated with the subseasonal EAWM precipitation is clearly evident, especially over the Indian Ocean, with the maximum precipitation anomalies located over the eastern Indian Ocean over 80–100°E from day 0 to day 5. In line with the eastward movement of convection, MJO-related moisture anomalies at 850 hPa also exhibit a systematic eastward propagation over the Indian Ocean (see contours in Fig. 2a; refer to Methods for details on how these MJO-related anomalous fields were extracted). Notably, the phase of moisture anomalies slightly leads precipitation anomalies by about 2–3 days, indicating the well-known process of moisture preconditioning during the MJO development. For example, prior to the onset of active MJO convection over the western equatorial Indian Ocean near 60°E, which occurs between day -10 and day -5, enhanced moisture anomalies associated with the MJO begin to emerge between day -15 and day -10 (Fig. 2a).

The evolution of vertical moisture profiles associated with the MJO over the western Indian Ocean is further illustrated in Fig. 2b (shaded), which closely aligns with the anomalous upward motion associated with the MJO (Fig. 2c, shaded). Notably, the onset of positive MJO moisture anomalies over the western Indian Ocean between day -15 and day -10 (Fig. 2b, shaded) tends to follow non-MJO moisture anomalies that peak ~10 days earlier (Fig. 2b, contours). These non-MJO moisture anomalies are closely linked to a peak of non-MJO anomalous upward motion in the lower troposphere between 850 hPa and 500 hPa (Fig. 2c contours), indicating that the initiation of the MJO over the western equatorial Indian Ocean can be triggered by the non-MJO circulation anomalies.

To further illustrate how the non-MJO circulation can initiate MJO convection over the western equatorial Indian Ocean, and taking into account the strongest signals in the non-MJO moisture (Fig. 2b) and vertical velocity (Fig. 2c) anomalies confined to the lower troposphere, Fig. 2d presents anomalous non-MJO winds (vectors), moisture (shaded), and vertical velocity derived based on the quasi-geostrophic equation[32,33] (QGω; contours) averaged between 850 and 500 hPa and from day -15 to day -10. The non-MJO low-level moistening during this period, which is critical for the MJO initiation as shown in Fig. 2b, is primarily evident over the Arabian Sea between the equator and 20°N, in the southeastern portion of a cyclonic circulation (Marked as "A") as part of a wave-train linked to the EAWM. Enhanced moisture in this region can be attributed to the QG upward motion over the eastern part of the cyclonic circulation "A" (Fig. 2d, contours) that is primarily driven by the warm temperature advection, and horizontal moisture advection by southerly anomalous winds (figures not shown). Since the MJO convection is largely driven by moisture anomalies as depicted by the "moisture mode" theory for the MJO[6,34], the increased moisture in the lower troposphere over the Arabian Sea is expected to facilitate the development of deep convection associated with the MJO, e.g., by reducing the dilution of rising thermal plums, thereby triggering the onset of the MJO. In contrast, over the northwestern part of the cyclone "A", which includes northwestern India, the Middle East, and East Africa, prevailing non-MJO anomalous downward QG motion and northerly winds lead to the drying of the lower troposphere.

A very similar cyclonic circulation pattern is observed over East Asia at this time ("Mark B", Fig. 2d). The dryness over the EAWM region is linked to downward QG vertical motion on the west of the cyclone, consistent with a suppressed phase of the EAWM precipitation (see Fig. 3, day -12). In contrast, a wet condition and associated enhanced precipitation occur over the western North Pacific (WNP) to the east of the Philippines, associated with QG upward motion in the southeast of the cyclonic circulation "B" (Fig. 2d). These findings clearly suggest that the initiation of MJO convection over the western equatorial Indian Ocean and the subseasonal variability of EAWM precipitation can be similarly influenced by Rossby wave disturbances along a zonally elongated wave-train pattern.

While the extratropical origin of the MJO has been suggested by previous studies, using either case studies[35,36] or model experiments[37–39], results in this study clearly demonstrate that a subtropical Rossby wave-train, when passing over the northern Indian Ocean, can trigger tropical MJO convection. Figure 2b indicates that the growth of MJO moisture perturbations over the western Indian Ocean tends to follow the peak phase of non-MJO moisture and vertical velocity anomalies; however, the detailed processes underlying the phase lag between the MJO and non-MJO moisture anomalies require further investigation. In addition to thermodynamic processes, there is also a possibility that the extratropical Rossby wave disturbances centered over the Arabian Sea, as shown in Fig. 2d, could directly induce equatorial Kelvin wave responses, potentially through a "Sverdrup effect", which could in turn trigger the initiation of MJO convection over the equatorial western Indian Ocean, as proposed by a recent idealized modeling study[40].

The global Rossby-wave pattern linking the EAWM with weather extremes worldwide

Considering the crucial role of the subtropical Rossby wave pattern in connecting tropical MJO activity over the Indian Ocean and the subseasonal variability of EAWM precipitation, we further examine the detailed characteristics of this subtropical Rossby wave-train in this section, particularly from a large-scale perspective. Figure 3 illustrates the global distribution of 500 hPa wind alongside surface precipitation and temperature anomalies linked to the evolution of subseasonal EAWM precipitation. It is clear that the subtropical Rossby wave pattern over the Asian sector, which connects

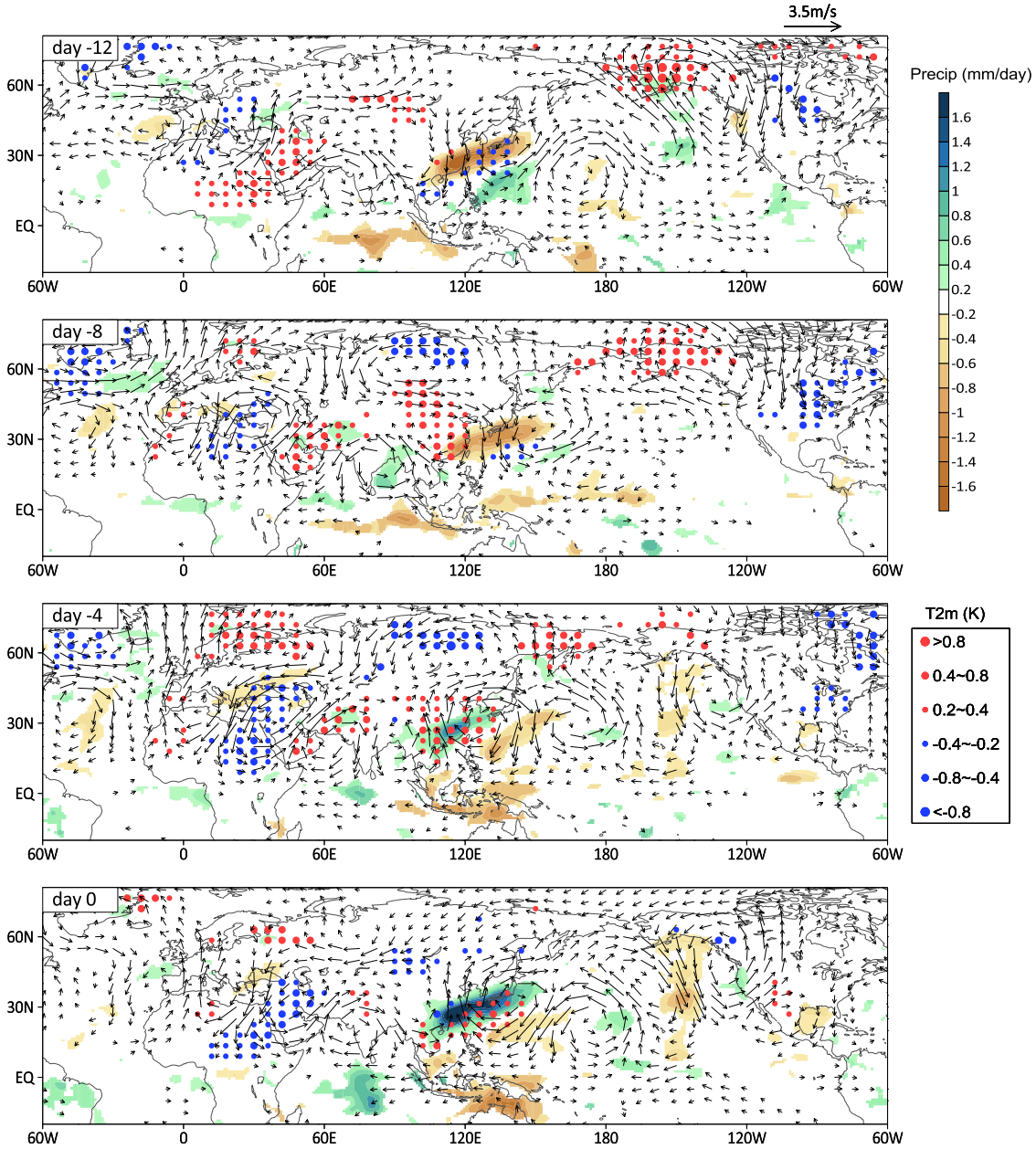

Fig. 3 | Global precipitation and temperature anomalies associated with subseasonal EAWM precipitation variability. Similar as for the left column in Fig. 1 but for total anomalous precipitation (shaded with units of mm day^{-1}, based on GPCP), wind at 500 hPa (vectors with speed less than 0.08 m s^{-1} omitted), and surface temperature (blue and red dots for positive and negative values; see the legend on the right). For precipitation and surface temperature, only anomalies surpassing the 95% statistical significance level are plotted.

MJO initiation over the Indian Ocean and the EAWM precipitation as previously discussed, is part of a global Rossby wave pattern featuring a wavenumber of 6. This Rossby wave pattern extends from the North Atlantic, traversing the Mediterranean Sea Region, India, East Asia, the North Pacific, and reaching all the way to North America and the Gulf of Mexico, largely following a waveguide along the subtropical westerly jet (Fig. 4). This wave pattern exhibits eastward propagation with a phase speed of about 3° per day over the Indo-Pacific sector (figure not shown). Given a wavelength of about 70 longitude degrees of the Rossby wave train in the Asian sector, determined by the distance between the two centers of cyclonic circulation masked as "A" and "B" in Fig. 2d, this propagation speed aligns well with the observed subseasonal period of ~25 days associated with EAWM precipitation variability.

While a strong link between the Rossby wave pattern and precipitation in the EAWM and tropical Indo-Pacific regions is again illustrated in Fig. 3 (shaded), widespread impacts of this Rossby wave pattern on precipitation anomalies extend well beyond the Indo-Pacific sector. These impacts can be observed in several areas, including the west coast of the Iberian Peninsula, the Mediterranean Sea Region, the North Pacific, Alaska, the west coast of North America, the Gulf of Mexico, and even in equatorial west Africa and the Amazon Basin in South America. For instance, during the peak phase of the subseasonal EAWM precipitation on day 0, reduced precipitation anomalies occur near the Mediterranean Sea Region, over the north Pacific and Alaska, and in the Gulf of Mexico. Conversely, enhanced precipitation is noted over the west coast of the Iberian Peninsula, in the west coast of North America, and in the Amazon Basin.

In addition to precipitation, this circumglobal Rossby wave pattern also significantly affects surface temperatures (color dots in Fig. 3). For instance, from day -12 to day 0, coinciding with the shift in EAWM precipitation from a negative to a positive phase, a patch of cold surface temperature anomalies

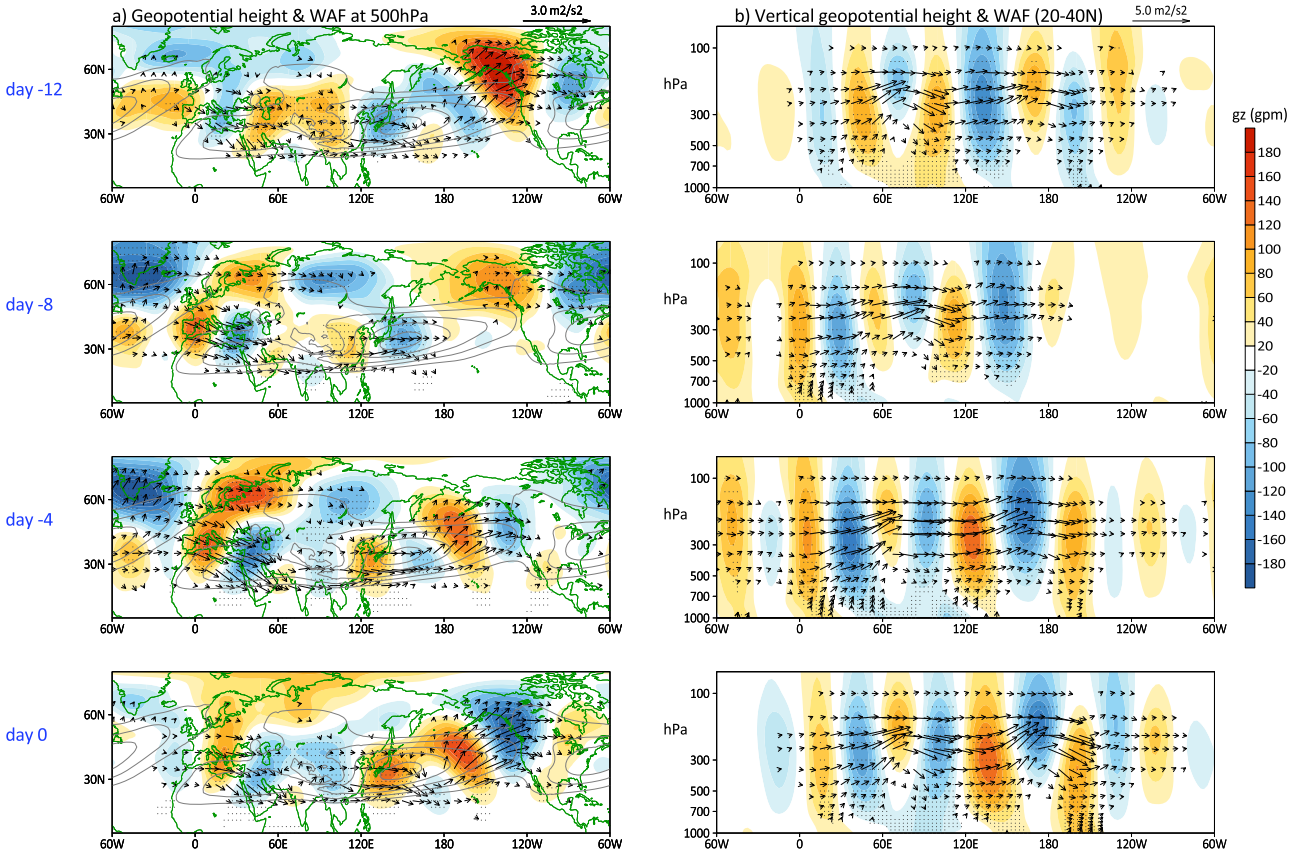

Fig. 4 | Energy sources of the Rossby wave-train along the subtropical jet. **a** Similarly as in Fig. 1a based on lead-lag regressions against EPC_1 of the leading subseasonal EAWM precipitation mode, but for evolution of geopotential height anomalies (shaded; color bar on the right with units of gpm) and associated horizontal wave activity fluxes at 500 hPa (vectors with the scale on the upper-right; amplitude less than 0.2 $m^2 s^{-2}$ omitted); (**b**) Evolution of pressure-longitude cross-sections of geopotential height anomalies (shaded) along with the vertical and zonal components of wave activity fluxes (vectors, see the scale on the upper-right with units of $m^2 s^{-2}$ for the horizontal and $10^{-3} m^2 s^{-2}$ for the vertical components, respectively). Variables in (**b**) are averaged over 25°–40°N where the subtropical westerly jet is located over the Eurasian sector. Areas with dark gray dots indicate anomalies surpassing the 95% statistical significance level for geopotential height anomalies.

gradually intensifies and moves southeastward from the Mediterranean Sea Region to the Middle East and North Africa. Additionally, on day -12 and day -8, a so-called "Warm Arctic-Cold Continent" pattern in surface temperature anomalies is discerned over North America, occurring alongside suppressed precipitation over East Asia. This "Warm Arctic-Cold Continent" pattern has been identified as a leading mode of subseasonal variability for wintertime surface temperatures over North America and plays a crucial role in influencing regional temperature extremes and Arctic sea ice[41–43].

To illustrate the energy sources sustaining the subseasonal circumglobal Rossby wave pattern, Fig. 4a shows the evolution of geopotential height (φ) anomalies and wave activity fluxes (WAF[44]; see "Methods") at 500 hPa associated with the subseasonal EAWM precipitation. It is evident that the alternating positive and negative φ anomalies along the wave train are primarily aligned with the subtropical jet stream waveguide (contours in Fig. 4a). Due to the presence of the Tibetan Plateau, the southward shift of the subtropical jet over the Indian sector creates a unique environment that interacts with the tropics, thereby initiating tropical MJO convection, as discussed earlier.

On day -12, the strongest φ anomalies and WAF are found over the North Pacific/North American sector; however, these anomalies significantly weaken afterwards. By day -8, wave disturbances in the Eurasian sector begin to intensify, associated with the formation of an anomalous high over the Iberian Peninsula and a strong injection of WAF into the entrance region of the subtropical jet near North Africa and the Mediterranean Sea Region. A strong divergence in WAF is seen over the west coast of the Iberian Peninsula on day -8 (Fig. 4a), with relatively weak wave fluxes from upstream. This suggests that the intensification of the Rossby wave-train downstream may be closely associated with the development of the anomalous high over the Iberian Peninsula. Additionally, the presence of positive φ anomalies over both the Iberian Peninsula and the western North Atlantic near 60°W, along with negative φ anomalies over Iceland at day -8, strongly resembles a positive phase of the North Atlantic Oscillation (NAO), indicating a potential role of the NAO in generating the circumglobal Rossby wave train along the subtropical jet stream. After day -8, the eastward propagation of the Rossby wave energy downstream along the subtropical jet becomes clearly apparent. By day 0, strong wave disturbances, which exhibit reversed signs compared to those observed on day -12, re-emerge over the North Pacific and North America (Fig. 4a).

The evolution of the Rossby wave pattern and the associated WAF is further illustrated in Fig. 4b by showing the vertical-longitude profiles of φ anomalies and WAF averaged over the latitude belt between 25°N and 40°N, where the subtropical jet stream is primarily located over the Eurasian sector. The downstream propagation of Rossby-wave energy, peaking around 250 hPa, and a gradual eastward amplification of wave disturbances are again clearly evident. It is particularly noteworthy that the relatively weak WAF in the central North Pacific on day -8 suggests that processes associated with the formation of the anomalous high over the Iberian Peninsula, a southern lobe of a positive NAO pattern, may play a critical role in energizing the downstream Rossby wave train along the subtropical jet.

Note that a zonally-extended Rossby wave pattern along the subtropical jet over the Eurasian sector during boreal winter has been widely

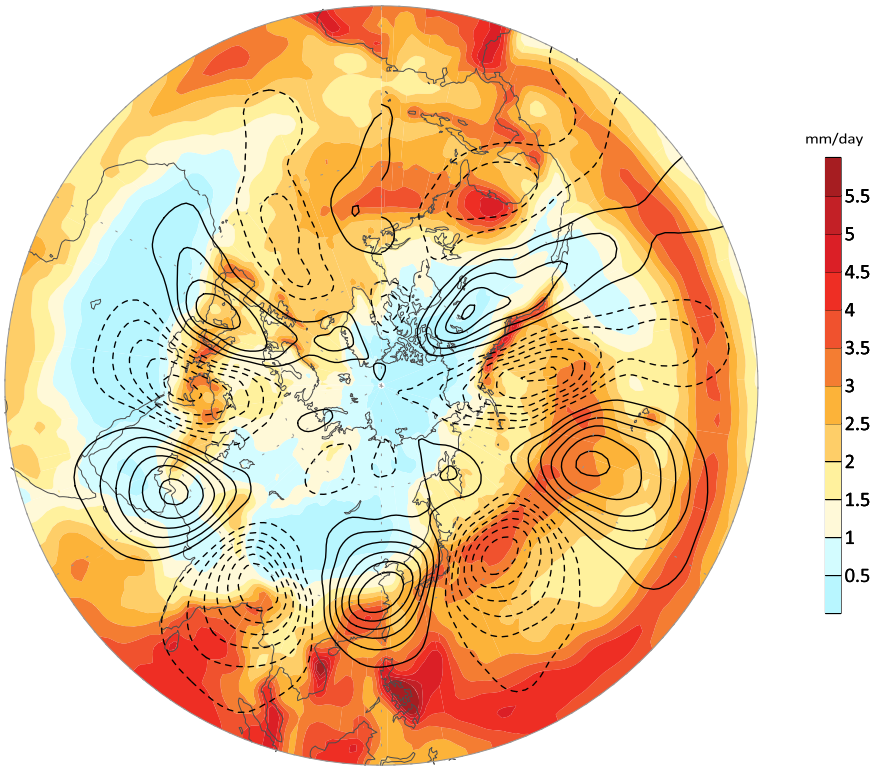

Fig. 5 | A schematic demonstrating the crucial role of the circumglobal Rossby wave pattern associated with the leading subseasonal variability mode of EAWM precipitation and the subseasonal-to-seasonal precipitation variability over global extratropics. Contours: the wavenumber-6 circumglobal Rossby wave pattern as represented by 300 hPa meridional v-wind anomalies based on regressions onto the EPC1 at day 0. Shaded: standard deviations of 10–30-day filtered daily precipitation during boreal winter (see the color bar). The selection of a band-pass filtering of 10–30 days here is based on the consideration of the prevailing period of about 25 days of the leading subseasonal precipitation variability mode over East Asia.

reported in the variability of monthly or seasonal mean circulation anomalies[45–50], or on the synoptic time-scale associated with extreme precipitation and temperature events over East Asia[51–55]. However, relatively few studies have examined the subseasonal variability of the Rossby wave train along the subtropical Asian jet and its impact on global precipitation during the boreal winter season. While the subseasonal Rossby wave pattern along the subtropical jet can generate the subseasonal variability of EAWM precipitation and the tropical MJO as shown in this study, previous studies suggest that the EAWM precipitation variability and the MJO itself could also play a crucial role in triggering and maintaining these extratropical Rossby wave patterns[56,57].

Discussion

Despite the urgent need for accurate S2S predictions to guide disaster preparedness and climate mitigation policy-making, our current S2S prediction skill remains limited, especially for precipitation, partially due to a lack of understanding of the key processes that govern regional S2S variability. Focusing on the S2S variability of winter precipitation over East Asia in this study, we illustrate that the leading subseasonal variability mode of EAWM precipitation is not only synchronized to MJO activity over the Indian Ocean, but is also closely linked to subseasonal variations of precipitation and surface temperature around the globe, through modulations by eastward-migrating Rossby wave-trains along the subtropical westerly jet. As further shown by Fig. 5, beyond the tropical region, where intense tropical convective variability occurs, the strongest subseasonal variability of precipitation in the extratropics is primarily observed along the latitudinal belt associated with the circumglobal Rossby wave pattern. This is particularly noticeable in regions influenced by local topography along coastal areas, such as the west coast of the Iberian Peninsula, the coastal regions around Mediterranean Sea Region, the Bay of Bengal, Southeast China, Japan, and the west coast of North America.

Particularly, the southward displacement of the subtropical westerly jet over the Indian region, influenced by the topographic effects of the Tibetan Plateau, creates a unique environment for the interaction between this subtropical Rossby wave-train and tropical convection. For instance, during the suppressed phase of subseasonal precipitation over the EAWM region, a lower-tropospheric trough is observed over the Arabian Sea around 20°N as part of the Rossby wave-train (Figs. 2d and 3a). Over the southeastern portion of the anomalous cyclonic circulation between the equator and 15°N, enhanced moisture anomalies are discerned, associated with quasi-geostrophic anomalous ascending motion resulting from warm temperature advection and horizontal moisture advection linked to the southwesterly anomalous winds (Fig. 2d). As a result, the MJO convection begins to develop over the western Indian Ocean, intensifying as it propagates eastward along the equator. After about 10 to 12 days, the previous cyclonic Rossby wave pattern over the Arabian Sea moves eastward into East Asia, leading to enhanced precipitation associated with the EAWM. At the same time, the MJO convection reaches the eastern Indian Ocean. This transition reveals a phase-locking between the heightened subseasonal precipitation in East Asia and the active MJO convection over the eastern Indian Ocean, as has been previously reported. However, a breakdown of the total subseasonal EAWM precipitation into an MJO-related component and a non-MJO component indicates that the MJO itself may only contribute up to 18% of total subseasonal EAWM precipitation variability. Despite the MJO's relatively minor role in influencing subseasonal EAWM precipitation, the predictability that it provides can still be valuable for making accurate S2S predictions of EAWM

In light of the profound influence of the circumglobal Rossby wave-train on the subseasonal variability of precipitation and temperature, these wave patterns can serve as critical sources of predictability for S2S predictions across extensive regions along the subtropical westerly jet. For instance, despite experiencing severe, prolonged droughts over the west coast of North America in recent years, our state-of-the-art climate models show limited skill for S2S predictions of winter precipitation in this area[12,58,59]. Historically, the El Niño-Southern Oscillation (ENSO) has been a primary factor for seasonal prediction of winter precipitation over the west coast of North America, with wet conditions during El Niño winters and dry conditions during La Niña winters[60,61]. However, the unexpectedly wet condition in California during the 2022/2023 winter coincided with a La Niña state over the eastern Pacific, which was not predicted by our major

prediction systems[59]. Recent analyzes indicate that the extremely wet condition over the west coast of North America during the 2022/2023 winter was closely linked to eastward-propagating Rossby wave disturbances from East Asia along the subtropical westerly jet[62], as discussed in this study. The connection between cross-Pacific short Rossby wave-trains, which are independent from ENSO, and the S2S variability of precipitation over the west coast of North America has also been documented in several recent studies[12,63,64]. This provides further evidence of the importance of circumglobal Rossby wave-trains for S2S predictions of global weather and climate extremes.

The results in this study suggest that the development of the circumglobal Rossby wave train related to the subseasonal variability of EAWM precipitation is closely tied to the formation of an anomalous high near the Iberian Peninsula, resembling a southern branch of the circulation anomalies during a positive phase of the NAO (Fig. 4, day -8). This thus indicates a potential pathway for NAO influences on the MJO via the circumglobal subtropical Rossby waves. However, the positive NAO-like pattern about eight days prior to the peak MJO convection over the eastern Indian Ocean (i.e., Wheeler-Hendon MJO Phase 3) as suggested in this study contradicts previous findings[65,66], which indicated that enhanced MJO convection over the Indian Ocean typically follows a negative phase of the NAO pattern over the Atlantic sector. Further investigations are needed to fully understand these discrepancies. One possible explanation is that the results of this study are associated with the subseasonal variability of EAWM precipitation; therefore, the NAO-like patterns and the MJO events captured here could represent only a small subset of all NAO and MJO events. This is supported by a sharp spectral peak around 25 days associated with the leading subseasonal EAWM precipitation mode (supporting Fig. S2), in contrast to a broad spectrum over the 20–50 days of the MJO (figure not shown), suggesting that part of MJO events could be independent from the subseasonal EAWM variability. Also, previous modeling studies have suggested that NAO conditions are not necessary for exciting the circumglobal Rossby waves[57,67]. It would be interesting to examine the percentage of MJO events over the IO initiated by the circumglobal subtropical Rossby waves, and the percentage of the circumglobal Rossby waves associated with the NAO.

While the subtropical circumglobal Rossby wave-train related to subseasonal EAWM precipitation shows largely similar characteristics to those previously reported for monthly or seasonal mean anomalies, differences in the Rossby wave patterns across various time scales are also evident. For example, while a global wavenumber-5 structure of the circumglobal Rossby wave train has been noted based on monthly or seasonal anomalous fields during boreal winter[46], this study identifies a wavenumber-6 pattern in the subseasonal Rossby-wave train (Fig. 3, also Fig. 5). As previously discussed, the unique wavelength (~70°) and propagation phase speed (3° per day) of the subseasonal Rossby wave pattern over the Indo-Pacific sector determine a prevailing time-scale of about 25 days for winter precipitation over East Asia. Therefore, the large-scale factors that influence the formation, amplitude, and phase of these subtropical circumglobal Rossby wave patterns on the subseasonal time scale may differ from those on monthly and seasonal time scales, necessitating further investigations. A better understanding of the origins and predictability of the subseasonal Rossby wave disturbances is essential for improving S2S predictions worldwide.

Caveats of this study are also noted, particularly regarding the method used to extract convection and circulation signals associated with the MJO based on lag-0 linear regressions. Previous research has indicated that extratropical responses to tropical convection can take one to 2 weeks to develop due to the propagation of the tropically excited Rossby waves into the extratropics[65,66,68,69]. Additionally, the responses in the extratropics to the MJO can be influenced by the large-scale mean state, such as the strength and location of the jet stream[45,68–72]. Consequently, the linear regression approach employed in this study may overlook MJO signals related to these nonlinear processes. Moreover, it is challenging to disentangle the interactive processes among the subseasonal EAWM variability, the subtropical Rossby wave-trains, and the MJO through observational analysis alone. Future studies should include numerical experiments to better understand the interactions among these systems.

Methods

Observational datasets

Daily variables from the European Centre for Medium-Range Weather Forecasts (ECMWF) ERA-5 reanalysis[73] are used to characterize large-scale patterns associated with the subseasonal variability of precipitation over East Asia. These valuables include surface air temperature, 3D geopotential height (φ), meridional and zonal winds (u, v), vertical velocity (w), and specific humidity (q) on 1.5° × 1.5° horizontal grids and 37 vertical pressure levels from 1000 to 1 hPa.

Daily precipitation data from the TRMM (version 3B42)[74] are used to extract the leading mode of the subseasonal variability of precipitation associated with the EAWM and the MJO. Precipitation from the Global Precipitation Climatology Project (GPCP)[75] is used to characterize global precipitation anomalies associated with the leading subseasonal variability mode of EAWM, considering its global coverage.

Analyses in this study mainly focus on the extended boreal winter from November to March during the period of 1998–2016. To extract the subseasonal variability signals, a 10−90-day band-pass filtering[76] is applied to daily anomalies of each variable after removal of the climatological annual cycle (annual mean plus three leading harmonics).

The leading subseasonal variability mode of the East Asia winter monsoon

Instead of an empirical orthogonal function (EOF) analysis used in many previous studies[17], we employ an extended EOF (EEOF) analysis[77,78] of 10–90 day filtered daily TRMM precipitation anomalies during the 1998–2016 winters (November–March) to identify the dominant subseasonal variability mode of EAWM precipitation. The EEOF is essentially the same as the EOF, just using an extended covariance matrix with the daily data during all these time lags. The EEOF analysis is conducted over the region of 17.5°–35°N and 95°E–140°E (see the red box in Fig.1a at day 0) with a time lag of 31 days. The derived eigenvectors based on the EEOF analysis, therefore, contain a series of evolution patterns of the leading modes. As shown in Figs. S1 and S2, the first and second modes ($EEOF_1$ and $EEOF_2$), with a same prevailing period of 25 days (0.04 cycle/day), explain about 4.9% and 4.7% of the total subseasonal precipitation variances, respectively, and thus represent the same leading subseasonal mode of the EAWM precipitation with a 90-° phase difference. In this study, various large-scale variables associated with the evolution of the leading subseasonal precipitation mode over East Asia are derived by lag regressions of their corresponding 10–90-day filtered anomalies against the principal component of the $EEOF_1$ (EPC_1).

Identification of the MJO and its associated signals

To examine the role of the MJO in contributing to the subseasonal variability of EAWM precipitation, we decompose the total anomalous precipitation pattern associated with the subseasonal EAWM precipitation variability (Fig. 1a) into two components: precipitation anomalies associated with the MJO (Fig. 1b) and dependent from the MJO (the non-MJO component; Fig. 1c), with the non-MJO precipitation anomalies derived by subtracting the MJO component from the total precipitation anomalies.

Since we focus on the remote influences of MJO convection on the EAWM, and considering the caveat of the Wheeler-Hendon MJO index due to blended low-frequency variability signals[79], we employ an EOF analysis of daily precipitation anomalies for 1998–2016 winters (November-March) to identify the dominant MJO convective signals. The EOF analysis of 10–90-day filtered TRMM precipitation anomalies is conducted over the equatorial Indo-Pacific region, 15°S–15°N, 40°–160°E, where MJO convection is most active. The two leading EOF modes capture typical anomalous rainfall patterns of the MJO at their different phases during its eastward

propagation, i.e., with enhanced MJO convection over the eastern equatorial Indian Ocean in EOF_1 and the Maritime Continent in EOF_2 (Supporting Fig. S3). The two leading principal components (PC_1 and PC_2) are then used to derive typical patterns of any 2D or 3D variable (Z) associated with the two leading EOF modes of the MJO by regressing the daily 10–90-day filtered anomalies of the variable (Z′) on to PC_1 and PC_2, and obtain their regressed patterns of $RegZ_1$ and $RegZ_2$ corresponding to the 1st and 2nd leading modes of the MJO, respectively. As an example, Supporting Fig. S4 illustrates regressed anomalous winds at 850 and 200 hPa, as well as geopotential height anomalies at 500 hPa onto the PC_1 time series. Anomalies of the variable Z associated with the MJO (Z'_{mjo}) on a particular day for 1998–2016 winters can then be derived by the regression patterns normalized by the amplitude of PC_1 and PC_2 on that day, i.e.,

$$Z'_{mjo} = RegZ_1 \times PC_1 + RegZ_1 \times PC_2$$

Meanwhile, anomalous fields that are independent of the MJO (i.e., the non-MJO component Z'_{non_mjo}) can be obtained by subtracting the MJO-related components (Z'_{mjo}) from the total 10–90-day filtered anomalies (Z′), i.e., $Z'_{non\_mjo} = Z' - Z'_{mjo}$. Note that a similar regression approach was used in ref. 17 to derive precipitation and circulation patterns associated with the MJO, but based on the Wheeler-Hendon MJO index. Supporting Fig. S5 illustrates standard deviations of daily precipitation during boreal winter associated with the MJO reconstructed using this approach, along with the percentage of the total variability of 10–90-day filtered precipitation anomalies explained by the MJO.

The evolution patterns of the variable Z, as well as its MJO and non-MJO components, associated with the leading subseasonal variability mode of EAWM precipitation can be further derived by lag-regressions of Z′, Z'_{mjo}, Z'_{non_mjo} against the time series of EPC_1, respectively, as shown in Fig. 1 for the precipitation and 850 hPa winds.

Wave activity flux (WAF)

An analysis of the 3D WAF is conducted to explore possible energy sources in sustaining the subtropical Rossby wave rain associated with the subseasonal variability of EAWM precipitation. The calculation of 3D WAF is based on the W-vector following Takaya and Nakamura[44], which is expressed as

$$\mathbf{W} = \frac{p}{2|\mathbf{U}|}\begin{Bmatrix} U\left(\psi_x'^2 - \psi'\psi'_{xx}\right) + V\left(\psi'_x\psi'_y - \psi'\psi'_{xy}\right) \\ U\left(\psi'_x\psi'_y - \psi'\psi'_{xy}\right) + V\left(\psi'^2_y - \psi'\psi'_{yy}\right) \\ \frac{f_0^2}{N^2}\left[U\left(\psi'_x\psi'_z - \psi'\psi'_{xz}\right) + V\left(\psi'_y\psi'_z - \psi'\psi'_{yz}\right)\right] \end{Bmatrix}$$

where ψ′ is the perturbation stream-function (ψ), derived based on lag-regressions of 10–90 day filtered ψ′ against the EPC_1 of the leading EAWM precipitation mode; U and V are winter mean zonal and meridional winds, respectively; f_0 is the Coriolis parameter; N^2 is the buoyancy frequency; p is the normalized pressure by 1000 hPa; and the subscripts represent partial derivatives in the corresponding x, y and z directions.

Data availability

The ERA5 data was downloaded from the website: https://cds.climate.copernicus.eu/datasets/reanalysis-era5-pressure-levels?tab=overview (10.24381/cds.bd0915c6). The daily GPCP precipitation data can be assessed at https://www.ncei.noaa.gov/products/climate-data-records/precipitation-gpcp-daily (DOI: 10.7289/V5RX998Z). The daily TRMM 3B42 precipitation data was downloaded from https://disc.gsfc.nasa.gov/datasets/TRMM_3B42_7/summary (DOI: 10.5067/TRMM/TMPA/3H/7).

Received: 26 October 2024; Accepted: 30 April 2025;
Published online: 16 May 2025

References

1. Intergovernmental Panel on Climate Change. In *Proc. climate Change 2021—The Physical Science Basis: Working Group I Contribution to the Sixth Assessment Report of the Intergovernmental Panel on Climate Change* (ed. Intergovernmental Panel on Climate) 1513–1766 (Cambridge University Press, 2023).
2. NASEM. Next Generation Earth System Prediction: Strategies for Subseasonal to Seasonal Forecasts, *National Research Council, National Academy of Sciences*, Engineering, and Medicine, Washington, DC, ISBN-978-0-309-38880-1, 290 pages (2016).
3. Vitart, F. & Robertson, A. W. The sub-seasonal to seasonal prediction project (S2S) and the prediction of extreme events. *npj Clim. Atmos. Sci.* **1**, https://doi.org/10.1038/s41612-018-0013-0 (2018).
4. Mariotti, A. et al. Windows of opportunity for skillful forecasts subseasonal to seasonal and beyond. *Bull. Am. Meteor. Soc.* **101**, E608–E625 (2020).
5. Madden, R. A. & Julian, P. R. Detection of a 40–50 day oscillation in the zonal wind in the tropical pacific. *J. Atmos. Sci.* **28**, 702–708 (1971).
6. Jiang, X. et al. Fifty years of research on the madden-julian oscillation: recent progress, challenges, and perspectives. *J. Geophys. Res. Atmos.* **125**, e2019JD030911 (2020).
7. Gibson, P. B. et al. Subseasonal-to-seasonal hindcast skill assessment of ridging events related to drought over the Western United States. *J. Geophys. Res. Atmos.* **125**, e2020JD033655 (2020).
8. Li, J., Li, F. & Wang, H. Subseasonal prediction of winter precipitation in southern China using the early November snowpack over the Urals. *Atmos. Ocean. Sci. Lett.* **13**, 534–541 (2020).
9. DeFlorio, M. J., Ralph, F. M., Waliser, D., Jones, J. & Anderson, M. L. Better subseasonal-to-seasonal forecasts for water management. *Eos*, **102**, https://doi.org/10.1029/2021EO159749 (2021).
10. Ham, S. & Jeong, Y. Characteristics of Subseasonal Winter Prediction Skill Assessment of GloSea5 for East Asia. *Atmosphere* **12**, 1311 (2021).
11. Sengupta, A. et al. Advances in Subseasonal to Seasonal Prediction Relevant to Water Management in the Western United States. *Bull. Am. Meteor. Soc.* **103**, E2168–E2175 (2022).
12. Jiang, X., Waliser, D. E., Gibson, P. B., Chen, G. & Guan, W. Why seasonal prediction of california winter precipitation is challenging. *Bull. Am. Meteor. Soc.* **103**, E2688–E2700 (2022).
13. Domeisen, D. I. V. et al. Advances in the subseasonal prediction of extreme events: relevant case studies across the globe. *Bull. Am. Meteor. Soc.* **103**, E1473–E1501 (2022).
14. Calì Quaglia, F., Terzago, S. & von Hardenberg, J. Temperature and precipitation seasonal forecasts over the Mediterranean region: added value compared to simple forecasting methods. *Clim. Dyn.* **58**, 2167–2191, https://doi.org/10.1007/s00382-021-05895-6 (2022).
15. Becker, E. J., Kirtman, B. P., L'Heureux, M., Muñoz, Á. G. & Pegion, K. A decade of the North American Multimodel Ensemble (NMME): research, application, and future directions. *Bull. Am. Meteor. Soc.* **103**, E973–E995 (2022).
16. Rivoire, P., Martius, O., Naveau, P. & Tuel, A. Assessment of subseasonal-to-seasonal (S2S) ensemble extreme precipitation forecast skill over Europe. *Nat. Hazards Earth Syst. Sci.* **23**, 2857–2871 (2023).
17. Yao, Y., Lin, H. & Wu, Q. Subseasonal variability of precipitation in China during boreal winter. *J. Clim.* **28**, 6548–6559 (2015).
18. Stephan, C. C. et al. A comprehensive analysis of coherent rainfall patterns in China and potential drivers. Part II: intraseasonal variability. *Clim. Dyn.* **51**, 17–33 (2018).
19. Yao, S., Tong, Q., Li, T. & Gong, K. The 10–30-day oscillation of winter rainfall in southern China and its relationship with circulation patterns in different latitudes. *Int. J. Climatol.* **40**, 3268–3280 (2020).
20. Wang, L., Jiang, J., Li, T., Zhou, X. & Chen, Z. Three distinct circulation patterns that induce enhanced intraseasonal precipitation events over South China in boreal winter. *Clim. Dyn.* **60**, 2893–2905 (2023).

21. Jeong, J.-H., Kim, B.-M., Ho, C.-H. & Noh, Y.-H. Systematic variation in wintertime precipitation in East Asia by MJO-induced extratropical vertical motion. *J. Clim.* **21**, 788–801 (2008).
22. Jia, X., Chen, L., Ren, F. & Li, C. Impacts of the MJO on winter rainfall and circulation in China. *Adv. Atmos. Sci.* **28**, 521–533 (2011).
23. He, J., Lin, H. & Wu, Z. Another look at influences of the Madden-Julian Oscillation on the wintertime East Asian weather. *J. Geophys. Res. Atmos.* **116**, https://doi.org/10.1029/2010JD014787 (2011).
24. Liu, Y. & Hsu, P.-C. Long-term changes in wintertime persistent heavy rainfall over southern China contributed by the Madden–Julian Oscillation. *Atmos. Ocean. Sci. Lett.* **12**, 361–368 (2019).
25. Zheng, Y., Zhang, Q., Luo, M., Sun, P. & Singh, V. P. Wintertime precipitation in eastern China and relation to the Madden-Julian oscillation: Spatiotemporal properties, impacts and causes. *J. Hydrol.* **582**, 124477 (2020).
26. Chen, Y.-L., Sui, C.-H., Chang, C.-P. & Tseng, K.-C. Effect of the MJO on East Asian Winter rainfall as revealed by an SVD analysis. *J. Clim.* **34**, 9729–9746 (2021).
27. Huffman, G. J., Adler, R. F., Rudolf, B., Schneider, U. & Keehn, P. R. Global precipitation estimates based on a technique for combining satellite-based estimates, rain-gauge analysis, and NWP model precipitation information. *J. Clim.* **8**, 1284–1295 (1995).
28. Wheeler, M. C. & Hendon, H. H. An all-season real-time multivariate MJO index: development of an index for monitoring and prediction. *Mon. Wea. Rev.* **132**, 1917–1932 (2004).
29. Chang, C. P., Liu, C. H. & Kuo, H. C. Typhoon Vamei: an equatorial tropical cyclone formation. *Geophys. Res. Lett.* **30**, 1150 (2003).
30. Jiao, Y. & Wu, R. Propagation and influence on tropical precipitation of intraseasonal variation over mid-latitude East Asia in boreal winter. *Atmos. Ocean. Sci. Lett.* **12**, 155–161 (2019).
31. Ma, T. et al. Linkage of strong intraseasonal events of the East Asian winter monsoon to the tropical convections over the Western Pacific. *Remote Sens.* **14**, 2993 (2022).
32. Nie, J., Dai, P. & Sobel, A. H. Dry and moist dynamics shape regional patterns of extreme precipitation sensitivity. *Proc. Natl. Acad. Sci. USA* **117**, 8757–8763 (2020).
33. Holton, J. R. *An Introduction to Dynamic Meteorology* 4th edn, (Academic Press 2008).
34. Adames, Á. F. & Maloney, E. D. Moisture mode theory's contribution to advances in our understanding of the Madden-Julian oscillation and other tropical disturbances. *Curr. Climate Change Rep.*, https://doi.org/10.1007/s40641-021-00172-4 (2021).
35. Hsu, H. H., Hoskins, B. J. & Jin, F. F. The 1985/86 intraseasonal oscillation and the role of the extratropics. *J. Atmos. Sci.* **47**, 823–839 (1990).
36. Wang, L., Kodera, K. & Chen, W. Observed triggering of tropical convection by a cold surge: implications for MJO initiation. *Quart. J. Roy. Meteor. Soc.* **138**, 1740–1750 (2012).
37. Ray, P., Zhang, C., Dudhia, J. & Chen, S. S. A numerical case study on the initiation of the Madden-Julian Oscillation. *J. Atmos. Sci.* **66**, 310–331 (2009).
38. Ray, P. & Li, T. Relative roles of circumnavigating waves and extratropics on the MJO and Its relationship with the mean state. *J. Atmos. Sci.* **70**, 876–893 (2013).
39. Lin, H., Brunet, G. & Derome, J. Intraseasonal variability in a dry atmospheric model. *J. Atmos. Sci.* **64**, 2422–2441 (2007).
40. Barpanda, P., Tulich, S. N., Dias, J. & Kiladis, G. N. The role of subtropical rossby waves in amplifying the divergent circulation of the Madden–Julian Oscillation. *J. Atmos. Sci.* **80**, 2377–2398 (2023).
41. Lin, H. Subseasonal variability of North American wintertime surface air temperature. *Clim. Dyn.* **45**, 1137–1155 (2015).
42. Guan, W. et al. The leading intraseasonal variability mode of wintertime surface air temperature over the North American sector. *J. Clim.* **33**, 9287–9306 (2020).
43. Guan, W., Jiang, X., Ren, X., Chen, G. & Ding, Q. Role of atmospheric variability in driving the "Warm-Arctic, Cold-Continent" pattern over the North America sector and sea ice variability over the Chukchi-Bering Sea. *Geophys. Res. Lett.* **47**, e2020GL088599 (2020).
44. Takaya, K. & Nakamura, H. A formulation of a phase-independent wave-activity flux for stationary and migratory quasigeostrophic eddies on a zonally varying basic flow. *J. Atmos. Sci.* **58**, 608–627 (2001).
45. Hoskins, B. J. & Ambrizzi, T. Rossby wave propagation on a realistic longitudinally varying flow. *J. Atmos. Sci.* **50**, 1661–1671 (1993).
46. Branstator, G. Circumglobal teleconnections, the jet stream waveguide, and the North Atlantic oscillation. *J. Clim.* **15**, 1893–1910 (2002).
47. Watanabe, M. Asian jet waveguide and a downstream extension of the North Atlantic Oscillation. *J. Clim.* **17**, 4674–4691 (2004).
48. Feldstein, S. B. & Dayan, U. Circumglobal teleconnections and wave packets associated with Israeli winter precipitation. *Quart. J. Roy. Meteor. Soc.* **134**, 455–467 (2008).
49. Hu, K., Huang, G., Wu, R. & Wang, L. Structure and dynamics of a wave train along the wintertime Asian jet and its impact on East Asian climate. *Clim. Dyn.* **51**, 4123–4137 (2018).
50. An, X. et al. Possible dynamic mechanisms of high- and low-latitude wave trains over Eurasia and their impacts on air pollution over the North China Plain in early winter. *J. Geophys. Res. Atmos.* **127**, e2022JD036732 (2022).
51. Zhou, W. et al. Synoptic-scale controls of persistent low temperature and Icy weather over southern China in January 2008. *Mon. Wea. Rev.* **137**, 3978–3991 (2009).
52. Wen, M., Yang, S., Kumar, A. & Zhang, P. An analysis of the large-scale climate anomalies associated with the snowstorms affecting China in January 2008. *Mon. Wea. Rev.* **137**, 1111–1131 (2009).
53. Li, C. & Sun, J. Role of the subtropical westerly jet waveguide in a southern China heavy rainstorm in December 2013. *Adv. Atmos. Sci.* **32**, 601–612 (2015).
54. Ding, F. & Li, C. Subtropical westerly jet waveguide and winter persistent heavy rainfall in south China. *J. Geophys. Res. Atmos.* **122**, 7385–7400 (2017).
55. Li, X. Maintenance of the South Asian jet wave train: eddy kinetic energy balance. *Clim. Dyn.* **57**, 687–700 (2021).
56. Zhou, F., Zhang, R. & Han, J. Influences of the East Asian summer rainfall on circumglobal teleconnection. *J. Clim.* **33**, 5213–5221 (2020).
57. Soulard, N., Lin, H., Derome, J. & Yu, B. Tropical forcing of the circumglobal teleconnection pattern in boreal winter. *Clim. Dyn.* **57**, 865–877 (2021).
58. Gibson, P. B. et al. Training machine learning models on climate model output yields skillful, interpretable seasonal precipitation forecasts. *Commun. Earth Environ.* **2**, 159 (2021).
59. DeFlorio, M. J. et al. From California's extreme drought to major flooding: evaluating and synthesizing experimental seasonal and subseasonal forecasts of landfalling atmospheric rivers and extreme precipitation during Winter 2022–2023. *Bull. Am. Meteor. Soc*. https://doi.org/10.1175/BAMS-D-22-0208.1 (2023).
60. L'Heureux, M. L., Tippett, M. K. & Barnston, A. G. Characterizing ENSO coupled variability and its impact on North American seasonal precipitation and temperature. *J. Clim.* **28**, 4231–4245 (2015).
61. Trenberth, K. E. et al. Progress during TOGA in understanding and modeling global teleconnections associated with tropical sea surface temperatures. *J. Geophys. Res. Oceans* **103**, 14291–14324 (1998).
62. Dong, C., Peings, Y. & Magnusdottir, G. Regulation of Southwestern United States precipitation by non-ENSO teleconnections and the impact of the background flow. *J. Clim.* **36**, 7415–7433 (2023).
63. Teng, H. & Branstator, G. Causes of extreme ridges that induce California droughts. *J. Clim.* **30**, 1477–1492 (2017).
64. Gibson, P. B. et al. Ridging associated with drought across the Western and Southwestern United States: characteristics, trends and predictability sources. *J. Clim.* **0**, null, https://doi.org/10.1175/jcli-d-19-0439.1 (2020).

65. Cassou, C. Intraseasonal interaction between the Madden-Julian Oscillation and the North Atlantic Oscillation. *Nature* **455**, 523–527 (2008).
66. Lin, H., Brunet, G. & Derome, J. An observed connection between the North Atlantic Oscillation and the Madden–Julian Oscillation. *J. Clim.* **22**, 364–380 (2009).
67. Huang, S., Li, X. & Wen, Z. Characteristics and possible sources of the intraseasonal South Asian jet wave train in boreal winter. *J. Clim.* **33**, 10523–10537 (2020).
68. Lin, H. & Brunet, G. Extratropical response to the MJO: nonlinearity and sensitivity to the initial state. *J. Atmos. Sci.* **75**, 219–234 (2018).
69. Jin, F. & Hoskins, B. J. The direct response to tropical heating in a baroclinic atmosphere. *J. Atmos. Sci.* **52**, 307–319 (1995).
70. Wang, J. et al. MJO teleconnections over the PNA region in climate models. Part I: performance- and process-based skill metrics. *J. Clim.* **33**, 1051–1067 (2020).
71. Henderson, S. A., Maloney, E. D. & Son, S.-W. Madden–Julian Oscillation pacific teleconnections: the impact of the basic state and mjo representation in general circulation models. *J. Clim.* **30**, 4567–4587 (2017).
72. Ting, M. & Sardeshmukh, P. D. Factors determining the extratropical response to equatorial diabatic heating anomalies. *J. Atmos. Sci.* **50**, 907–918 (1993).
73. Hersbach, H. et al. The ERA5 global reanalysis. *Quart. J. Roy. Meteor. Soc.* **146**, 1999–2049 (2020).
74. Kummerow, C. et al. The status of the Tropical Rainfall Measuring Mission (TRMM) after two years in orbit. *J. Appl. Meteor.* **39**, 1965–1982 (2000).
75. Huffman, G. J. et al. Global precipitation at one-degree daily resolution from multisatellite observations. *J. Hydrometeorol.* **2**, 36–50 (2001).
76. Duchon, C. E. Lanczos filtering in one and two dimensions. *J. Appl. Meteorol. Climatol.* **18**, 1016–1022 (1979).
77. Weare, B. C. & Nasstrom, J. S. Examples of extended empirical orthogonal function analyses. *Mon. Weather Rev.* **110**, 481–485 (1982).
78. Jiang, X. & Waliser, D. E. Northward propagation of the subseasonal variability over the eastern Pacific warm pool. *Geophys. Res. Lett*. **35**, https://doi.org/10.1029/2008GL033723 (2008).
79. Lyu, M., Jiang, X. & Wu, Z. A cautionary note on the long-term trend in activity of the Madden-Julian Oscillation during the past decades. *Geophys. Res. Lett.* **46**, 14063–14071 (2019).

Acknowledgements

J.X. and R.Z. are supported by the National Natural Science Foundation of China (42288101). X.J. acknowledges support by the Regional and Global Model Analysis Program of US Department of Energy under Award DE-SC0024315.

Author contributions

J.X., X.J., and R.Z. designed the research; J.X. carried out analyses under the guidance of X.J. and R.Z.; J.X., X.J., and R.Z. wrote the paper.

Competing interests

The authors declare no competing interests.

Additional information

Supplementary information The online version contains supplementary material available at https://doi.org/10.1038/s41612-025-01076-y.

Correspondence and requests for materials should be addressed to Xianan Jiang or Renhe Zhang.